Available online at www.sciencedirect.com
SCIENCE DIRECT®
Journal of volcanology and geothermal research
ELSEVIER
Journal of Volcanology and Geothermal Research 129 (2004) 125–138
www.elsevier.com/locate/jvolgeores

Predicting yield strengths and effusion rates of lava domes from morphology and underlying topography

Aaron W. Lyman [a,*], Elissa Koenig [b], Jonathan H. Fink [b]

[a] *Research School of Earth Sciences, Australian National University, Canberra, ACT 0200, Australia*
[b] *Department of Geological Sciences, Arizona State University, Box 871404, Tempe, AZ 85287-1404, USA*

Received 29 May 2002; received in revised form 16 December 2002; accepted 18 December 2002

Abstract

To investigate the effects of slope on the morphology of lava domes, laboratory experiments were conducted with a PEG–kaolin slurry erupted into cold water on slopes ranging from 0 to 60°. In each experiment the slope, effusion rate, and water temperature were varied, producing four distinct morphologies: spiny, lobate, platy, and no-crust. Each morphology is correlated with Ψ_B and slope, where Ψ_B is defined as the ratio of the timescale of solidification to the timescale of advection. As the underlying slope increases from 0 to 40°, each morphology forms at a lower value of Ψ_B than it would on a horizontal surface. Above 40°, the transitions between morphologies become independent of slope and the platy morphology is no longer observed. Once a range of Ψ_B values for a dome is determined based on its morphology and slope, its yield strength or effusion rate can be calculated. In the case of active domes, observations of the effusion rate can be used to calculate yield strength, while for prehistoric domes an assumption of yield strength based on composition is used to determine the effusion rate. For active domes we estimate yield strengths of $0.4–7.3\times10^5$ Pa, and effusion rate ranges for prehistoric domes of 0.1–330 $m^3\ s^{-1}$. These values compare well with yield strengths of $1.0–2.0\times10^5$ Pa measured in the laboratory and effusion rates of 0.1–40 $m^3\ s^{-1}$ observed during historically active dome eruptions.

Keywords: yield strength; lava dome; laboratory experiments; effusion rate

1. Introduction

In the last century lava domes have become recognized as one of the most hazardous volcanic phenomena, both in terms of frequency and difficulty to predict. Collapsing lava domes and associated explosions have claimed many lives and destroyed extensive amounts of property. Predicting when, where, and how quickly a lava dome may advance is critical to assessing its hazard potential.

Previous work by Griffiths and Fink (1997) and Fink and Griffiths (1998) has shown that the morphology of lava domes can be related to their eruption conditions and explosive hazard. They used laboratory experiments to reproduce the growth of such domes and found that four distinct morphologies formed repeatedly over a range of initial conditions. The final morphology

* Corresponding author. Tel.: +61-02-6125-9961; Fax: +61-02-6125-0315.
E-mail address: aaron.lyman@anu.edu (A.W. Lyman).

0377-0273/03/$ – see front matter © 2003 Elsevier B.V. All rights reserved.
doi:10.1016/S0377-0273(03)00236-1

and the initial conditions could be related through a dimensionless parameter that encompassed the eruption rate, magma rheology, and thickness of the cooling surface. They also found that this relationship could be used to estimate the yield strength of an active dome, provided that its effusion rate could be measured, and the effusion rates of prehistoric flows, based on their composition.

One variable that previous studies have not included is underlying slope. In most cases lava domes erupt in the bottom of explosion craters (e.g. Soufrière of St. Vincent and Mount St. Helens) and do not traverse steep slopes. However, occasionally domes grow large enough to overtop crater walls and are able to then travel down the flank of a volcano (e.g. Mount Unzen and Colima volcano). In other instances dome lobes are emplaced on top of each other (e.g. Mount St. Helens and Montserrat) and can encounter very steep (up to 50 or 60°) local slopes. In this study, we have conducted ninety-seven experiments on slopes ranging from 0–60° to evaluate the effects of this variable on dome morphology and to see how it affects the calculation of yield strength and effusion rate using the method outlined in Fink and Griffiths (1998).

2. Laboratory simulations

2.1. Scaling relationships

Griffiths and Fink (1997) showed that flow morphology could be predicted from the ratio of the timescale of solidification to the timescale of advection. This dimensionless ratio, Ψ_B can be written:

$$\Psi_B = \frac{t_s}{t_a} \tag{1}$$

where t_s is the time needed for the magma surface to cool from its erupted temperature to its solidification temperature and t_a is the time required for the flow to advance a distance equal to its thickness. t_s can be written in the form:

$$t_s = \lambda\, \tau_s(\Theta_s) \tag{2}$$

where λ is the dimensionless timescale through which the slurry's surface temperature decreases from the vent temperature and approaches the ambient water temperature (Griffiths and Fink, 1997).

$$\lambda = 100\pi \left(\frac{\rho c}{\rho_a c_a}\right)^2 \left(\frac{v_a}{g\alpha_a \Delta T}\right)^{\frac{2}{3}} \kappa_a^{-\frac{4}{3}} \kappa \tag{3}$$

The dimensionless temperature difference, Θ_s, through which the lava surface must cool before solid begins to form, is given by:

$$\Theta_s = \frac{(T_s - T_a)}{(T_l - T_a)} \tag{4}$$

where T_s is the temperature of solidification for the slurry, T_a is the ambient water temperature, and T_l is the temperature of the slurry at the vent (Fink and Griffiths, 1990). The dimensionless parameter, $\tau_s(\Theta_s)$, can be fit (for $\Theta_s > 0.4$) by the polynomial expression (Griffiths and Fink, 1997):

$$\tau_s(\Theta_s) = e^{-1}[8.8694 + 40.443 \ln\Theta_s + 135.89(\ln\Theta_s)^2 + 294.24(\ln\Theta_s)^3 + 364(\ln\Theta_s)^4 + 236.08(\ln\Theta_s)^5 + 62.111(\ln\Theta_s)^6] \tag{5}$$

The time of advection can be expressed as:

$$t_a = \frac{h_0}{U} \tag{6}$$

where h_0 is the height scale and U is the velocity scale. For Bingham materials (Blake, 1990), h_0 is defined as:

$$h_0 = \frac{\sigma_0}{g\Delta\rho} \tag{7}$$

and U is defined as:

$$U = \frac{Q}{h_0^2} \tag{8}$$

where g is gravitational acceleration, $\Delta\rho$ is the density difference between the magma and the environment into which it erupts, σ_0 is the isothermal yield strength and Q is the volumetric effusion rate. Combining Eqs. 1–8 gives an expression for Ψ_B:

$$\Psi_B = (g\Delta\rho/\sigma_0)^3 Q t_s \tag{9}$$

Since Ψ_B is dimensionless, it can be evaluated for both laboratory and natural domes.

2.2. Laboratory set-up and procedures

Laboratory experiments were conducted using a slurry of polyethylene glycol (PEG 600) wax and kaolin clay in a 1.155:1 ratio, to simulate the rheology of silicic lava domes. Previous laboratory experiments (Fink and Griffiths, 1990, 1992) with solidifying wax made use of this grade of polyethylene glycol because of its solidification temperature (18–20°C, depending on batch and trace water content), density greater than water, and its viscosity ($\sim 1.6\times10^{-4}$ m^2 s^{-1}) which is sufficiently high to give small Reynolds numbers for the flows (Griffiths and Fink, 1997). PEG 600 was used in these experiments because of its solidification temperature. The ratio of PEG 600 to kaolin clay (1.155:1) was chosen to create a slurry with a yield strength ($\sim$100 Pa) and density ($\sim$1500 kg m^{-3}) great enough to support a dome 2–4 cm high, making it possible to make measurements of the dome and to ensure that the flows were dominated by strength as opposed to viscous stresses (Griffiths and Fink, 1997).

The PEG–kaolin slurry was thoroughly mixed at room temperature (21–22°C), then placed into a glass cylinder (Fig. 1). One end of the cylinder was connected to the base of a tank by a small tube, while the other was connected to a water reservoir via another tube and a positive-displacement peristaltic pump. An acrylic piston that slid on a single O-ring separated the slurry and water in the cylinder. The rate at which the slurry was extruded into the bottom of the tank was controlled by and assumed to equal the rate at which water was pumped into the back of the cylinder.

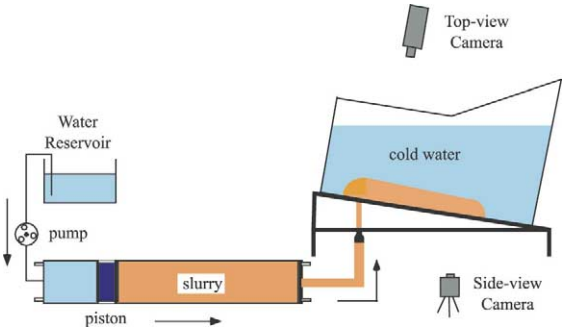

Fig. 1. Schematic drawing of the laboratory set-up. Water pumped from a reservoir into the back of a glass cylinder pushes a piston forward, expelling slurry through a tube and on to the base of the tank, which can be set at angles of 0–60°.

The slurry was extruded into the base of a tank tilted at the desired angle and filled with chilled water (Fig. 1). The chilled water causes the surface of the slurry to freeze, simulating the solidification of lava. Effusion rates of the slurry were 0.6–3.7$\times10^{-6}$ m^3 s^{-1}, eruption temperature of the slurry was assumed to be room temperature (21–22°C), water temperatures varied from 2 to 24°C, and the slope of the tank could be set between 0 and 60°.

Each experiment was run until at least 500 cm^3 of slurry was extruded or until the flow reached one of the tank walls, which can last from 5 to 20 min depending on effusion rate, slope, and water temperature. Each experiment was videotaped using two Hi8 video cameras, one placed over the top of the tank perpendicular to the base, and one placed perpendicular to the side of the tank. Still frames were captured from the videotapes and used to record the height and length of each experiment as a function of time or volume. Visual inspection of each experiment was used to classify dome morphology and Eq. 9 was used to calculate Ψ_B (Fig. 2).

2.3. Experimental results

Spiny domes (Fig. 2a) form at the lowest Ψ_B values, where effusion rate and water temperature are both low. This results in spine-like lobes that emerge from the vent in a manner similar to that of an up-heaved plug. They grow vertically from the vent until they are unable to support their weight and collapse to the side. As more lava is added, the pile grows taller with newer spines punctuating the top. Spines have smooth sides that may have grooves parallel to the direction of flow caused by extrusion through the jagged solidified surface of the dome.

Lobate domes (Fig. 2b) form at slightly higher Ψ_B values. Lobate domes initially grow through inflation of a solidified crust (Griffiths and Fink,

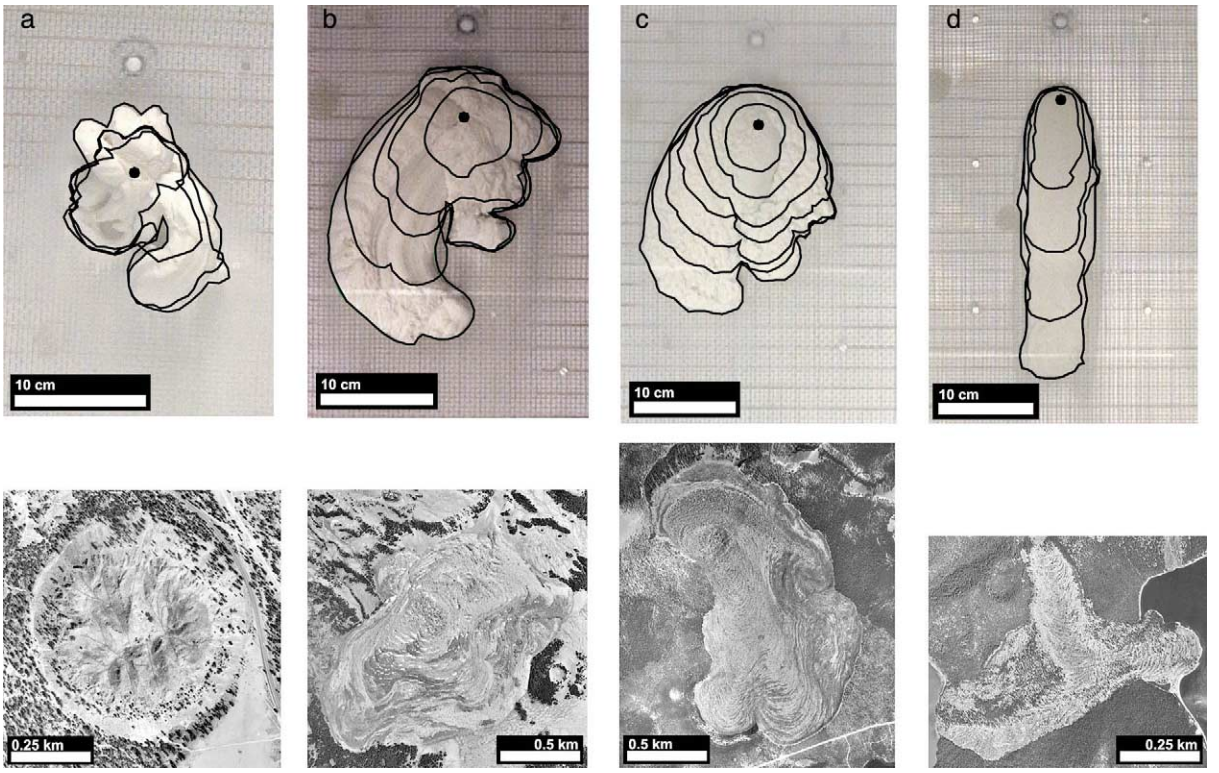

Fig. 2. Top views of the four morphologies, i.e. spiny, lobate, platy, and no-crust, as displayed by experimental (top) and natural flows (bottom). (a) Experiment AL-013 ($\Psi_B = 0.07$, Slope = 10°) and Wilson Butte, CA ($\Psi_B = 0.01$–0.10, Slope = 4.26°). (b) Experiment AL-031 ($\Psi_B = 0.44$, Slope = 20°) and Rock Mesa, OR ($\Psi_B = 0.10$–1.25, Slope = 7.56°). (c) Experiment AL-034 ($\Psi_B = 1.45$, Slope = 20°) and Big Obsidian Flow, CA ($\Psi_B = 0.40$–2.85, Slope = 10.31°). (d) Experiment AL-014 ($\Psi_B = 4.62$, Slope = 30°) and Inter-lake Flow, OR ($\Psi_B = 0.10$–1.02, Slope = 11.85°). In the images of experiments the lines indicate the flow outline at volume increments of 125 ml and the circles indicate vent locations.

1997), but after a short time lobes begin to break out laterally because the weaker lava is less able to support vertical spines. Lobate domes commonly have four to six arms that grow outward in a radial fashion. Each lobe continues to grow until a weaker spot in the dome carapace appears, through which a new lobe emerges. Only one lobe grows at a time and occasionally old lobes are reactivated. The thickness of a lobe is approximately equal to its width. Lobes typically have smooth sides and wave-like ridges when they extrude through the solidified carapace of the dome.

Platy domes (Fig. 2c) form at the next higher range of Ψ_B values. This morphology consists of rigid plates of solidified slurry underlain and separated by flowing masses of unsolidified slurry. In contrast to spiny and lobate domes, platy domes have rough surfaces because they are not extruded through or past any solidified material and extension caused by advance of the flow is sufficient to fracture the crust. Solidified plates can help control the direction of growth by becoming fixed to the base of the tank and acting as a barrier to the advancing flow.

Domes formed at the highest Ψ_B values (Fig. 2d) do not develop any crust except at their outermost margins. This may be because the water is not cold enough to cause the surface of the dome to freeze or the rate of advance is high enough that any crust that starts to form is sheared apart. These domes tend to be much wider than they are tall and can resemble pancakes.

On slopes less than 40°, the transitions between morphologies occur at lower Ψ_B values as slopes

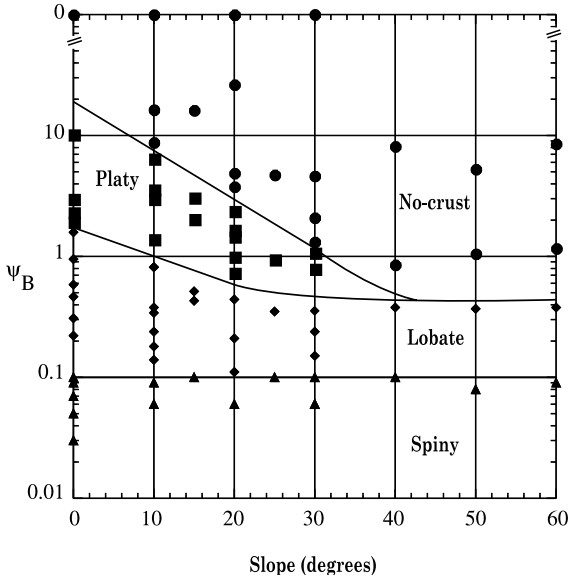

Fig. 3. Plot showing the range of Ψ_B values for which a given morphology forms. Each experiment is classified according to the style of flow: circles, no solid or only solid levees at the flow front (referred to as 'no-crust'); squares, solid plates over most of the surface and eventual extrusion of ridges from the divergent plate boundaries (referred to as 'platy'); diamonds, extruding lobes classified as 'lobate'; and triangles, extruding spines classified as 'spiny'.

increase. Above 40°, these transitions become independent of slope and the platy morphology is no longer observed (Fig. 3). Equations for the transitions between morphologies were found by fitting exponential curves to the boundaries separating each morphology and are given in Table 1 along with the range of Ψ_B values given by Fink and Griffiths (1998) for flows on a horizontal surface. The platy morphology becomes indistinguishable from the no-crust morphology at higher slopes because the surface carapace of the flow is continually sheared apart, preventing plates or levees from forming. However, the lobate and spiny morphologies continue to form at higher slopes because the rate of crust growth is high enough to prevent total disruption of the carapace. Gregg and Fink (2000) found that PEG flows on slopes above 40° were also sheared apart and unable to maintain a coherent flow.

3. Determining Ψ_B of natural domes

Dome morphology and underlying slope are required to calculate Ψ_B for natural domes. Aerial photography, ground photography, or direct observations are used to look for features analogous to those described in Section 2 to classify dome morphology. Domes that are transitional between two different morphologies are classified as both (e.g. spiny–lobate) and assigned intermediate values of Ψ_B (Table 1). The slope beneath a dome is calculated using standard structural geologic methods to find the attitude of a plane passing through three points near the edge of the dome. The X, Y, and Z positions of these points are located using GPS measurements, digital elevation maps (DEMs), or topographic maps. Once the morphology and underlying slope have been determined, the equations in Table 1 are used to calculate the range of Ψ_B values and corresponding emplacement conditions that would have produced the dome.

For this study, 10-m-resolution DEMs were used to calculate the slopes beneath domes in the Inyo volcanic chain, South Sister volcano,

Table 1
Range of possible Ψ_B values for a given morphology on a horizontal plane (Fink and Griffiths, 1998) and on slopes up to 30°

	Fink and Griffiths, 1998		This study	
Type	Ψ_B Min	Ψ_B Max	Ψ_B Min	Ψ_B Max
Spiny	0.01	0.12	0.01	0.10
Spiny–Lobate	0.03	0.30	0.04	$0.03+0.59e^{(-0.05*\beta)}$
Lobate	0.12	0.90	0.10	$1.78e^{(-0.05*\beta)}$
Lobate–Platy	0.30	3.00	$0.03+0.59e^{(-0.05*\beta)}$	$0.59e^{(-0.05*\beta)}+6.32e^{(-0.09*\beta)}$
Platy	0.90	15.00	$1.78e^{(-0.05*\beta)}$	$18.97e^{(-0.09*\beta)}$
Platy–No-crust	3.00	30.00	$0.59e^{(-0.05*\beta)}+6.32e^{(-0.09*\beta)}$	$33.33+6.32e^{(-0.09*\beta)}$
No-crust	15.00	–	$18.97e^{(-0.09*\beta)}$	–

and Newberry Crater and 30-m-resolution DEMs were used for domes in the Medicine Lake Highland volcano. Measurements of the slopes beneath active domes were taken from published sources.

4. Applications to active domes: estimating yield strength

4.1. Method

Eq. 9 can be used to calculate the yield strength of an active dome provided that morphology, underlying slope, composition and effusion rate are known. Ψ_B is determined from the observed dome morphology and underlying slope, following methods described in Section 3. Composition is used to determine density and solidification timescale for the dome lava (Table 2). Effusion rate is defined as the change in volume divided by the time between volume measurements (i.e. $Q = dV/dt$). One way of approximating the volume of a dome is with the equation $V = C\pi R^2 H$, where H and R are the height and radius of the dome, respectively, and C is a proportionality constant (C would be 2/3 for a perfect hemisphere). Height and radius can be measured in the field using visual estimates, electronic distance measuring devices, and GPS receivers. Another way of calculating the change in volume is by subtracting volumes calculated using two DEMs created from topographic maps and aerial photographs at different times (Stevens et al., 1997).

Table 2
Material constants used in calculations

Composition	SiO_2[a] (%)	ρ[b] (kg m^{-3})	t_s[c] (s)	σ_0[c] (10^5 Pa)
Rhyolite	>68	2400	32	3.0
Rhyodacite		2450	50	2.5
Dacite	63–68	2500	65	2.0
Silicic andesite		2550	78	1.5
Andesite	57–63	2600	90	1.0
Basaltic andesite	52–56	2650	150	0.5

[a] Cas and Wright, 1987.
[b] Basalt (Griffiths and Fink, 1992); andesite and rhyolite (Murase and McBirney, 1973); dacite (Anderson and Fink, 1992).
[c] Fink and Griffiths, 1998.

Young et al. (1997) developed a new method of creating DEMs by using helicopters equipped with laser range finding binoculars to survey 15–30 points distributed over the dome. The collected data are then used to generate a new DEM. DEMs can also be generated from synthetic aperture radar data (Stevens et al., 2001). A slightly different method to calculate effusion rates of active flows, developed by Harris et al. (1998), uses a thermal model and input parameters based on data from the Landsat Thematic Mapper and the Advanced Very High Resolution Radiometer. The change in time dt, is simply the time elapsed between two volume measurements.

For this study we have identified five recent eruptions where a dome was extruded onto slopes greater than 5°, and morphologies, compositions, and emplacement rates are known: Mount Unzen, Japan; Mount St. Helens, Washington; Santiaguito, Guatemala; Merapi, Indonesia; and Soufrière Hills, Montserrat. This information is then used to calculate the yield strengths of these domes.

4.2. Mount Unzen example

Here we use the eruption of Mount Unzen to illustrate how our approach can be used to estimate the yield strength of an active dome (Fig. 4). From the onset of emplacement in May 1991 until it ceased in 1995, the dome grew both through inflation and by extruding many small lobes (Fig. 4). The eruption has been divided into two stages, each lasting about two years (Nakada et al., 1999). During the first stage, most of the lava erupted higher up on the volcano where slopes were approximately 17° (Nakada et al., 1999) and had a lobate morphology. During the second stage, the dome reached a steeper part of the volcano where the underlying slope was closer to 31° (Nakada et al., 1999), and the morphology was spiny–lobate. Using the slope measurements and morphology information along with Table 1, we calculate minimum and maximum Ψ_B values of 0.10 and 0.79, respectively, for the first stage of the eruption, and 0.17 and 0.52 for the second one.

Effusion rates of 2.50 m^3 s^{-1} and 1.14 m^3 s^{-1}

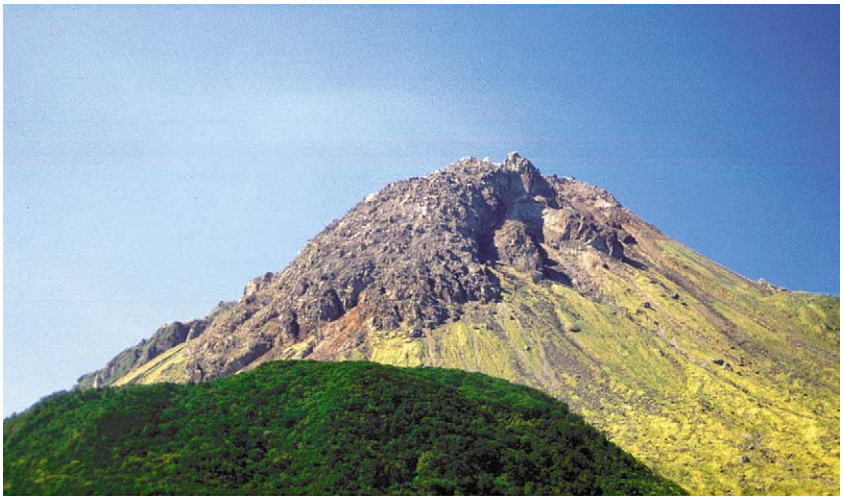

Fig. 4. Mount Unzen, Japan (photo by Chris Eisinger, 2000). View is to the southwest of the largest lobe, lobe 11, which grew between March and October 1994 (Nakada et al., 1999).

were calculated based on average effusion rates from Nakada et al. (1999) for the first and second stages of the eruption, respectively. Values for $\Delta\rho$ and t_s were taken from Table 2 based on a dacitic composition (Nakada and Motomura, 1999). Using Eq. 9 with these numbers and the calculated Ψ_B values, gives yield strengths between 1.4×10^5 Pa and 2.9×10^5 Pa for the first stage of the eruption and 1.9×10^5 Pa to 3.1×10^5 Pa for its second stage.

4.3. Results

This same approach has been used to calculate yield strengths for the four other domes mentioned earlier. Table 3 shows the yield strength estimates from this study along with calculations assuming zero slopes. The values predicted from this study are $0.4–7.3\times10^5$ Pa, which compares well with previously published yield strengths of intermediate to silicic lavas (Blake, 1990; Hulme, 1974; Murase et al., 1985; Fink and Griffiths, 1998). The yield strengths calculated using slope differ only slightly from the values calculated for the same domes without slope (Table 3). Ψ_B decreases slightly when slope is used in its determination (Fig. 3), but not enough to affect the yield strength calculations. Effusion rate has the great-

Table 3
Yield strength estimates for several historically active lava domes

Dome	Time period or extrusion type	Morphology	Slope	Ψ_B range		σ_0 range (10^5 Pa)	
				With slope	Without slope	With slope	Without slope
Merapi	1994–1995	Platy	29	0.45–1.37	0.9–15	0.36–0.52	0.26–0.66
Montserrat	1995–1996	Spiny	31	0.01–0.10	0.01–0.12	1.95–4.21	1.84–4.21
	1996–1997	Spiny–Lobate	31	0.04–0.17	0.03–0.63	2.65–4.40	1.17–4.71
	1997–1998	Spiny–Lobate	23	0.04–0.23	0.03–0.30	3.64–6.73	3.34–7.2
Mount St. Helens	Dome	Lobate	5	0.10–1.41	0.12–0.90	0.72–1.73	0.83–1.63
	Lobes	Lobate	5–36	0.10–1.51	0.12–0.90	0.96–7.29	1.93–3.77
Santiaguito	Domes	Spiny	1	0.01–0.10	0.01–0.12	1.15–2.48	1.08–2.48
	Block flows	Lobate	30	0.04–0.18	0.03–0.30	0.55–0.94	0.74–1.59
Unzen	1991–1993	Lobate	17	0.10–0.79	0.12–0.90	1.44–2.88	1.39–2.71
	1993–1995	Spiny–Lobate	31	0.04–0.17	0.03–0.30	1.86–3.10	1.54–3.31

est effect on the calculation of yield strength when using Eq. 9.

Fig. 5 is a plot of calculated yield strength vs. SiO_2 content for the five active domes described in this paper, plus Soufrière of St. Vincent (Lyman, 2001), Mount Pinatubo (Fink and Griffiths, 1998), Redoubt (Fink and Griffiths, 1998), and laboratory measurements of the Mount St. Helens dacite (Murase et al., 1985). Past studies have attempted to link yield strength to SiO_2 content (Bottinga and Weill, 1972; Hulme, 1974), and Fig. 5 shows a slight correlation. However, other factors have been recognized as influencing lava yield strength, such as vesicularity and crystallinity (Fink and Griffiths, 1998; Saar et al., 2001; Varga et al., 1990).

In the case of Montserrat and Mount Unzen, where data exist for multiple stages of dome growth, a progressive increase in yield strength is shown (Table 3). This could be a result of crystallization of magma within the chamber, gas loss, or a decline in effusion rate.

5. Applications to prehistoric domes: estimating effusion rate

5.1. Method

Sampling of prehistoric domes allows direct measurements of lava yield strengths (Murase et al., 1985), but eruption rates are indeterminate. Eq. 9 can also be used to calculate the effusion rate of a prehistoric dome provided that morphology, underlying slope, and composition are known. In addition, if a dome's volume is known, dividing it by the estimated effusion rate, Q can constrain the eruption duration. This calculation

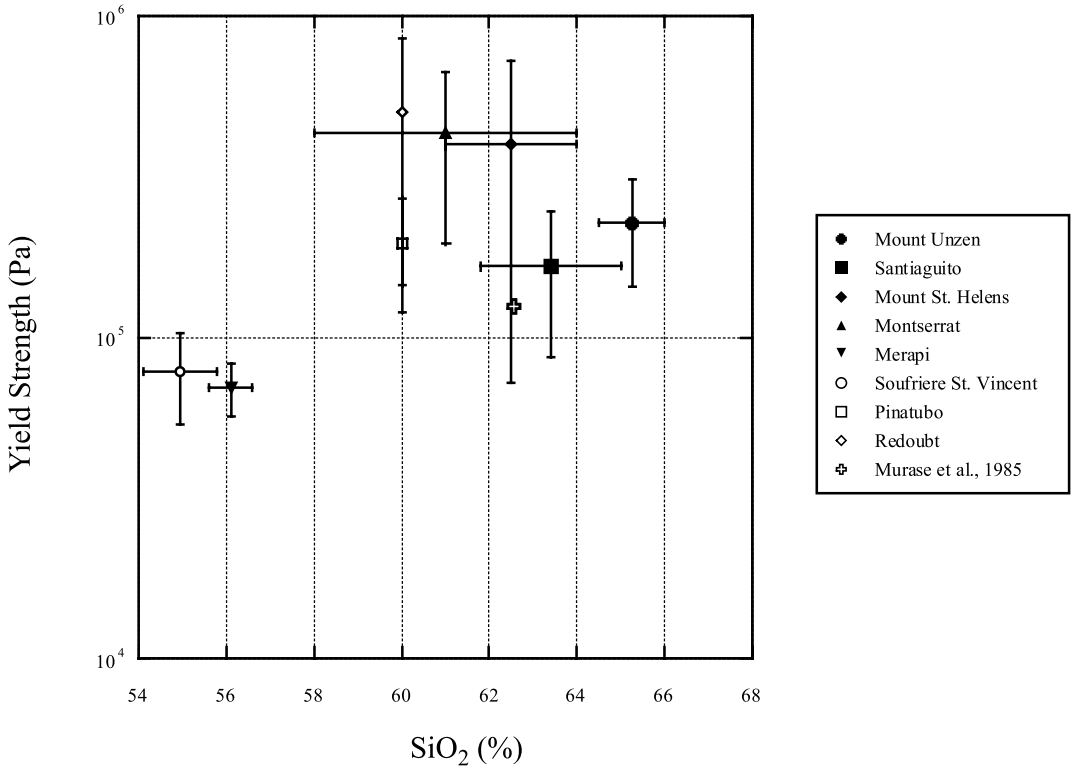

Fig. 5. Plot of yield strengths for several domes active in historic time. The error bars show the range in values of SiO_2 content in the X direction and the range of yield strengths in the Y direction. These ranges take into account all estimates for each dome except for the Murase et al. (1985) value, which is a laboratory measurement based on the dacite of Mount St. Helens.

assumes a constant effusion rate and continuous eruption. Because most dome eruptions have episodic or decreasing effusion rates, the durations calculated in this manner tend to underestimate the actual duration and should be considered rough estimates only.

We estimate effusion rates and eruption durations for domes at South Sister volcano, Oregon; Newberry Crater, Oregon; Medicine Lake Highland volcano, California; Inyo Volcanic Chain, California, and the Chao Dacite Flow, Chile (Table 4).

5.2. Big Obsidian Flow example

Here we use the Big Obsidian Flow (Fig. 6) within Newberry Crater to illustrate how Eq. 9 can be used to determine the effusion rate of a prehistoric lava flow. First, we need to classify the morphology of the dome and determine its underlying slope. The Big Obsidian Flow covers the central section of Newberry Crater, flowing from the south wall of the caldera, northward toward its center. It is composed of several lobes that spread into more platy structures on shal-

Table 4
Effusion rate and eruption duration estimates of several prehistoric lava domes, and estimates from other methods

	Morphology	Slope	Ψ_B range	Effusion Rate			Volume	Eruption duration
				This study Q (m^3 s^{-1})	A and F[a] Q (m^3 s^{-1})	F and G[b] Q (m^3 s^{-1})	(km^3)	(days)
South Sister								
DH2	Spiny	15.58	0.01–0.10	0.2–2	6	3.2	0.01	26–261
DH3	Spiny	8.42	0.01–0.10	0.2–2	19	3.2	0.04	195–1952
DH4	Spiny	3.58	0.01–0.10	0.2–2	14	3.2	0.02	97–969
DH5	Spiny–Lobate	12.88	0.04–0.36	0.8–8			0.04	58–560
Miller Flow	Lobate–Platy	9.47	0.40–3.06	25447			0.06	27668
Newberry Flow	Lobate–Platy	17.41	0.29–1.57	12966		12	0.20	65–351
Rock Mesa	Lobate	7.56	0.10–1.25	46784			0.50	206–2568
Newberry Volcano								
Inter-lake Flow	Lobate	11.85	0.10–1.02	24259			0.13	23–232
East-side Domes	Lobate–Platy	3.59	0.53–5.07	35–328			0.05	1–6
Big Obsidian Flow	Lobate–Platy	10.31	0.40–2.85	26–184			0.16	4–73
Medicine Lake								
Little Glass Mountain	Lobate	1.91	0.10–1.63	6–105			0.30	33–536
Crater Glass	Lobate–Platy	3.96	0.53–4.91	34–318			0.10	4–34
Dacite Flow	Platy–Axi	1.97	5.83–38.62	49–323			0.10	4–24
Big Glass Dacite	Lobate–Platy	1.00	0.60–6.34	5–73			0.80	127–1336
Big Glass Rhyolite	Lobate	8.00	0.10–1.22	6–79			0.20	29–358
Inyo								
Wilson Butte	Spiny	4.26	0.01–0.10	0.6–6			0.05	89–894
Obsidian Dome Dacite	Platy	4.22	1.46–12.95	12–108		7	0.13	14–123
Obsidian Dome Rhyolite	Spiny	4.22	0.01–0.10	0.6–6		2	0.04	72–715
Glass Creek North Side	Lobate–Platy	8.12	0.44–3.44	28–223			0.05	1–7
Glass Creek South Side	Platy	22.5	0.61–2.48	40–161			0.05	4–15
Deadman	Lobate	3.53	0.10–1.51	6–98			0.13	15–232
Chao								
Stage I	Platy	20	0.69–3.11	6–26		1.5–10[c]	11.00	4901–22135
Stage II	Lobate–Platy	10.00	0.40–2.93	3–24			9.00	4257–30953
Stage III	Lobate	5.00	0.10–1.41	1–12			3.00	2955–41566
Stage IV	Lobate	3.00	0.10–1.55	1–13			3.00	2682–41566

[a] Anderson and Fink, 1992.
[b] Fink and Griffiths, 1998.
[c] Manley, 1996.

Fig. 6. Aerial photograph of Big Obsidian Flow, Newberry Crater. Flow traverses an average slope of 10° and overtops an older pumice cone at the top right. The flow has lobate structures where the slopes are steeper, but spreads out more and develops a platy morphology as the flow reaches lower slopes.

lower slopes, classifying it as a lobate–platy dome. To determine the underlying slope, we find the X, Y, and Z coordinates of three points near the edge of the dome from DEMs. A lobate–platy morphology, along with a calculated slope of 10.31° gives minimum and maximum Ψ_B values of 0.4 and 2.85, respectively (Table 1).

Values of g and σ_0, $\Delta\rho$, and t_s, are obtained from Table 2 based on composition. Laidley and McKay (1971) report silica contents for the Big Obsidian Flow of 72%, giving it a rhyolite composition. Therefore, we assign values of 3.0×10^5 Pa, 2400 kg m^{-3}, and 32 s, for the yield strength, density, and solidification timescale, respectively. Using these values along with Eq. 9 we calculate effusion rates between 26 and 180 m^3 s^{-1}. Using a volume of 0.16 km^3 (Laidley and McKay, 1971) and the range of effusion rates, we calculate an eruption duration between 4 and 73 days.

5.3. Results

The effusion rates calculated in the previous example are up to an order of magnitude higher than have been observed for recently active lava domes, and the eruption duration is correspondingly short. Eq. 9 shows that effusion rate is proportional to the yield strength cubed and therefore the yield strength has the largest effect on the effusion rate calculation. The yield strength used

in the effusion rate estimate for Big Obsidian Flow is based on its SiO_2 content. However, the flow has a very low crystallinity (Kathy Cashman, pers. commun., 2002) compared to the domes in Section 5.2, which can result in the lava having a much lower yield strength than its composition would suggest. If we recalculate the effusion rates with yield strengths of 2.0 and 1.0 $\times 10^5$ Pa, we estimate effusion rates between 8–55 $m^3\ s^{-1}$ and 1–7 $m^3\ s^{-1}$, and corresponding eruption durations between 35–250 days and 275–2000 days, respectively.

It is difficult to assign an appropriate range of effusion rates for lava domes, since eruptions of rhyolite domes have not been witnessed. Estimates of effusion rates have come from laboratory studies similar to the one presented in this paper (Fink and Griffiths, 1998), measurements of crease structures (Anderson and Fink, 1992), measurements of bubble shapes (Rust et al., 2002; Castro et al., 2002), and cooling models (Manley, 1996). Most measured effusion rates are for domes that have spiny or lobate morphologies, which according to the laboratory experiments should have low effusion rates. Recent data for the Popocatépetl dome shows that it has a no-crust morphology and measured effusion rates of 180–200 $m^3\ s^{-1}$ (Wunderman et al., 2000). This would suggest that effusion rates on the order of 10^2 are possible for lava domes. Further work on measuring the yield strength of prehistoric lavas is needed for the method of estimating effusion rates presented here to be practical.

6. Conclusions

In this study we have explored the effects of slope on the morphology of lava domes, which can be used to calculate yield strength and effusion rate (Fink and Griffiths, 1998). Including slope affects the range of Ψ_B values that will produce a certain morphology. As the underlying slope increases from 0 to 40° each morphology forms at a lower value of Ψ_B than it would on a horizontal surface. Above 40°, the transitions between morphologies become independent of slope and the platy morphology is no longer observed.

Accounting for slope in the calculations of yield strength and effusion rate has little effect on the values predicted. The yield strengths and effusion rates calculated using slope differ only slightly from the values calculated for the same domes without slope. Ψ_B decreases slightly when slope is used in its determination, but not enough to affect the yield strength or effusion rate calculations. Effusion rate has the greatest effect on the calculation of yield strength when using Eq. 9. Similarly, yield strength has the greatest effect on effusion rate calculations and more precise knowledge of the yield strength of lava domes is needed for the method of estimating effusion rates presented here to be practical.

Acknowledgements

Reviews by Steven Blake and Michael Manga helped improve this manuscript. Research was supported by grant NAGW529 from NASA's Planetary Geology and Geophysics Program, NSF grant EAR0001015, and by the Scion Natural Science Association.

Appendix 1

Parameter values and flow regime for each experiment

Experiment number	Slope β	Temp. slurry (°C)	Temp. ambient (°C)	Effusion rate ($m^3\ s^{-1} \times 10^{-6}$)	Morphology type	t_A (s)	λ	θ_S	τ_S	t_s (s)	Ψ_B
AL-001	0	25.0	11.8	2.52E-6	P	3.536	52.938	0.591	0.129	6.843	1.94
AL-002	0	25.5	10.9	3.36E-6	P	2.652	50.247	0.597	0.122	6.142	2.32
AL-003	0	25.0	15.3	3.36E-6	P	2.652	61.031	0.443	0.450	27.442	10.35
AL-004	0	23.0	8.0	1.68E-6	L	5.304	52.113	0.773	0.022	1.169	0.22
AL-005	0	25.0	12.7	2.94E-6	P	3.031	54.590	0.561	0.168	9.145	3.02
AL-006	0	24.3	10.9	2.10E-6	L	4.243	53.193	0.651	0.076	4.040	0.95
AL-007	0	24.5	1.8	5.38E-7	S	16.575	44.281	0.784	0.020	0.875	0.05
AL-008	20	25.1	10.8	1.68E-6	P	5.304	51.111	0.615	0.104	5.323	1.00
AL-009	20	25.9	16.3	3.70E-6	NC	2.411	60.372	0.344	1.052	63.528	26.35
AL-010	20	24.2	13.2	2.52E-6	P	3.536	58.280	0.582	0.140	8.155	2.31
AL-011	20	24.0	12.9	3.19E-6	P	2.791	58.245	0.604	0.116	6.734	2.41
AL-012	20	23.3	13.4	2.52E-6	P	3.536	62.295	0.626	0.095	5.889	1.67
AL-013	20	25.0	3.8	6.72E-7	L	13.260	44.688	0.745	0.031	1.365	0.10
AL-014	30	22.5	15.8	3.36E-6	NC	2.652	77.413	0.567	0.159	12.298	4.64
AL-015	30	23.5	12.5	2.52E-6	NC	3.536	59.024	0.645	0.080	4.695	1.33
AL-016	30	23.5	7.0	1.68E-6	L	5.304	49.810	0.764	0.025	1.247	0.24
AL-017	30	23.0	9.5	2.10E-6	P	4.243	54.389	0.748	0.030	1.611	0.38
AL-019	10	24.0	12.0	2.52E-6	P	3.536	56.206	0.633	0.089	4.987	1.41
AL-020	10	24.0	7.8	1.68E-6	L	5.304	49.689	0.728	0.036	1.805	0.34
AL-022	10	23.0	20.9	2.52E-6	NC	3.536	153.658	−0.619	Infinite	Infinite	Infinite
AL-024	10	23.5	22.4	2.52E-6	NC	3.536	230.744	−2.545	Infinite	Infinite	Infinite
AL-025	30	23.8	22.6	2.52E-6	NC	3.536	223.289	−2.609	Infinite	Infinite	Infinite
AL-026	0	24.0	22.7	2.52E-6	NC	3.536	205.436	−2.385	Infinite	Infinite	Infinite
AL-027	20	23.5	20.9	2.52E-6	NC	3.536	133.266	−0.500	Infinite	Infinite	Infinite
AL-028	20	23.0	15.9	2.52E-6	NC	3.536	74.346	0.521	0.235	17.437	4.93
AL-030	20	25.0	7.8	2.52E-6	P	3.536	47.743	0.686	0.055	2.614	0.74
AL-031	20	25.0	4.7	2.52E-6	L	3.536	45.249	0.734	0.034	1.553	0.44
AL-032	20	24.0	23.1	2.52E-6	NC	3.536	260.845	−3.889	Infinite	Infinite	Infinite
AL-034	20	24.0	12.1	2.52E-6	P	3.536	56.418	0.630	0.091	5.146	1.46
AL-035	40	24.0	16.0	2.52E-6	NC	3.536	68.538	0.450	0.424	29.083	8.23
AL-036	40	25.0	10.3	1.68E-6	NC	5.304	50.640	0.633	0.089	4.521	0.85
AL-037	40	25.0	3.5	6.72E-7	S	13.260	44.515	0.749	0.029	1.309	0.10
AL-038	20	23.0	21.6	2.52E-6	NC	3.536	199.041	−1.429	Infinite	Infinite	Infinite
AL-039	20	23.5	15.0	2.52E-6	NC	3.536	67.005	0.541	0.198	13.284	3.76
AL-040	20	24.0	2.8	6.22E-7	S	14.335	45.511	0.792	0.018	0.812	0.06
AL-041	20	23.8	2.7	2.52E-6	L	3.536	45.737	0.801	0.016	0.733	0.21
AL-042	10	25.0	17.3	3.36E-6	NC	2.652	68.716	0.299	0.623	42.828	16.15
AL-043	15	25.0	17.3	3.36E-6	NC	2.652	68.716	0.299	0.623	42.828	16.15
AL-045	10	24.0	23.0	3.70E-6	NC	2.411	243.537	−3.400	Infinite	Infinite	Infinite
AL-046	10	25.0	15.0	3.36E-6	NC	2.652	60.125	0.460	0.390	23.430	8.84
AL-047	10	25.0	12.3	3.36E-6	P	2.652	53.827	0.575	0.149	8.005	3.02
AL-048	15	25.0	11.0	3.36E-6	P	2.652	51.649	0.614	0.105	5.432	2.05
AL-049	0	26.0	4.6	2.52E-6	L	3.536	43.765	0.701	0.048	2.081	0.59
AL-051	10	24.0	15.0	1.93E-6	P	4.612	64.500	0.511	0.255	16.440	3.56
AL-051	10	24.0	15.0	1.93E-6	P	4.612	64.500	0.511	0.255	16.440	3.56
AL-052	10	24.0	11.0	1.93E-6	L	4.617	54.265	0.662	0.069	3.728	0.81
AL-052	10	24.0	11.0	1.93E-6	L	4.612	54.265	0.662	0.069	3.728	0.81
AL-054	10	24.1	16.0	1.93E-6	P	4.612	67.973	0.444	0.445	30.261	6.56
AL-056	30	24.5	11.0	2.10E-6	P	4.243	52.917	0.637	0.086	4.541	1.07
AL-057	30	24.5	5.0	6.72E-7	L	13.260	46.224	0.749	0.029	1.361	0.10
AL-060	40	22.5	11.0	1.93E-6	L	4.617	58.887	0.748	0.030	1.751	0.38
AL-061	50	23	16.4	1.93E-6	NC	4.617	77.367	0.485	0.317	24.502	5.31
AL-062	50	23	13.3	1.93E-6	NC	4.617	63.263	0.649	0.077	4.851	1.05

Appendix I (*Continued*).

Experiment number	Slope β	Temp. slurry (°C)	Temp. ambient (°C)	Effusion rate ($m^3\ s^{-1} \times 10^{-6}$)	Morphology type	t_A (s)	λ	θ_S	τ_S	t_s (s)	Ψ_B
AL-064	50	23	8.2	5.88E-7	S	15.154	52.389	0.770	0.023	1.217	0.08
AL-065	50	23	10.0	1.84E-6	L	4.843	55.266	0.738	0.033	1.812	0.37
AL-066	60	23	8.7	5.88E-7	S	15.154	53.114	0.762	0.025	1.351	0.09
AL-067	60	23	9.9	1.93E-6	L	4.617	55.085	0.740	0.032	1.769	0.38
AL-069	60	23.5	12.9	1.93E-6	NC	4.617	60.062	0.632	0.090	5.390	1.17
AL-070	60	23.5	16.7	1.93E-6	NC	4.617	75.442	0.426	0.522	39.377	8.53
AL-071	30	25	10.0	1.68E-6	P	5.304	50.237	0.640	0.084	4.198	0.79
AL-072	30	25	14.9	8.47E-7	NC	10.520	59.834	0.465	0.373	22.290	2.12
AL-073	25	25	5.8	1.68E-6	L	5.304	46.025	0.719	0.040	1.841	0.35
AL-074	25	25.2	10.5	1.68E-6	P	5.304	50.455	0.619	0.101	5.087	0.96
AL-075	25	25.2	15.0	1.68E-6	NC	5.304	59.336	0.451	0.421	24.968	4.71
AL-076	15	24	15.0	1.68E-6	P	5.304	64.500	0.511	0.255	16.440	3.10
AL-077	15	24	8.9	1.68E-6	L	5.304	51.033	0.709	0.044	2.254	0.43
AL-078	15	24	9.8	1.68E-6	P	5.304	52.298	0.690	0.053	2.756	0.52
AL-079	25	23.2	2.4	1.68E-6	S	5.304	46.429	0.827	0.011	0.520	0.10
AL-080	15	23.2	2.7	1.68E-6	S	5.304	46.626	0.824	0.012	0.542	0.10
AL-081	0	24	4.3	5.88E-7	S	15.154	46.502	0.777	0.022	1.004	0.07
AL-082	30	24.1	2.9	5.88E-7	S	15.154	45.428	0.788	0.019	0.859	0.06
AL-083	0	27.1	2.4	4.20E-7	S	21.215	41.403	0.696	0.050	2.057	0.10
AL-084	10	27.4	2.6	2.52E-7	S	35.359	41.142	0.685	0.055	2.265	0.06
AL-085	10	27.2	3.0	3.36E-7	S	26.519	41.516	0.686	0.055	2.275	0.09
AL-086	10	27.3	1.9	1.68E-6	L	5.304	41.010	0.697	0.049	2.028	0.38
AL-087	10	27.3	3.7	8.40E-7	L	10.608	41.681	0.674	0.061	2.560	0.24
AL-088	10	27.2	2.0	6.22E-7	L	14.335	41.152	0.698	0.049	2.005	0.14
AL-089	10	27.1	3.0	7.06E-7	L	12.628	41.630	0.689	0.053	2.221	0.18
AL-090	30	26.7	2.9	2.52E-7	S	35.359	42.056	0.702	0.047	1.986	0.06
AL-091	30	26.2	1.4	9.07E-7	L	9.822	42.048	0.734	0.034	1.445	0.15
AL-092	30	26.9	2.9	1.68E-6	P	5.304	41.822	0.696	0.050	2.088	0.39
AL-093	0	25.5	4.0	1.68E-6	L	5.304	44.110	0.726	0.037	1.649	0.31
AL-094	0	25.0	3.4	5.88E-7	S	15.154	44.458	0.750	0.029	1.291	0.09
AL-095	0	27.0	4.0	1.68E-6	L	5.304	42.171	0.678	0.059	2.483	0.47
AL-096	0	25.0	2.2	2.35E-7	S	37.885	43.831	0.763	0.025	1.103	0.03
AL-097	0	24.3	11.0	3.36E-6	L	2.652	53.446	0.647	0.079	4.207	1.59

The morphologies are classified in column 6 as No-crust (NC), Platy (P), Lobate (L), and Spiny (S).

References

Anderson, S.W., Fink, J.H., 1992. Crease structures: Indicators of emplacement rates and surface stress regimes of lava flows. Geol. Soc. Am. Bull. 104, 615–625.

Blake, S., 1990. Viscoplastic models of lava domes. In: Fink, J.H. (Ed.), Lava Flows and Domes: Emplacement Mechanisms and Hazard Implications. Springer, New York, pp. 88–126.

Bottinga, Y., Weill, D.F., 1972. The viscosity of magmatic silicate liquids: A model for calculation. Am. J. Sci. 272, 438–475.

Cas, R.A.F., Wright, J.V., 1987. Volcanic Successions Modern and Ancient. Allen and Unwin, Boston, 528 pp.

Castro, J.M., Manga, M., Cashman, K.V., 2002. Dynamics of obsidian flows inferred from microstructures: Insights from microlite preferred orientations. Earth Planet. Sci. Lett. 199, 211–226.

Fink, J.H., Griffiths, R.W., 1990. Radial spreading of viscous-gravity currents with solidifing crust. J. Fluid. Mech. 221, 485–509.

Fink, J.H., Griffiths, R.W., 1992. A laboratory analog study of the surface morphology of lava flows extruded from point and line sources. J. Volcanol. Geotherm. Res. 54, 19–32.

Fink, J.H., Griffiths, R.W., 1998. Morphology, eruption rates, and rheology of lava domes: Insights from laboratory models. J. Geophys. Res. 103, 527–545.

Gregg, T.K.P., Fink, J.H., 2000. A laboratory investigation into the effects of slope on lava flow morphology. J. Volcanol. Geotherm. Res. 96, 145–159.

Griffiths, R.W., Fink, J.H., 1992. The morphology of lava flows in planetary environments: Predictions from analog experiments. J. Geophys. Res. 97, 19739–19748.

Griffiths, R.W., Fink, J.H., 1997. Solidifying Bingham extrusions; a model for the growth of silicic lava domes. J. Fluid. Mech. 347, 13–36.

Harris, A.J.L., Flynn, L.P., Keszthelyi, L., Mouginis-Mark, P.J., Rowland, S.K., Resing, J.A., 1998. Calculation of lava effusion rates from Landsat TM data. Bull. Volcanol. 60, 52–71.

Hulme, G., 1974. The interpretation of lava flow morphology. Geophys. J. R. Astron. Soc. 39, 361–383.

Laidley, R.A., McKay, D.S., 1971. Geochemical examination of obsidians from Newberry Caldera, Oregon. Contrib. Mineral. Petrol. 30, 336–342.

Lyman, A., 2001. The Effects of Slope on the Growth and Collapse of Lava Domes. M.Sc. Thesis, Arizona State University, Tempe, AZ.

Manley, C.R., 1996. Physical volcanology of a voluminous rhyolite lava flow: The Badlands lava, Owyhee Plateau, southwestern Idaho. J. Volcanol. Geotherm. Res. 71, 129–153.

Murase, T., McBirney, A.R., 1973. Properties of some common igneous rocks and their melts at high temperatures. Geol. Soc. Am. Bull. 84, 3563–3592.

Murase, T., McBirney, A.R., Melson, W.G., 1985. Viscosity of the dome of Mount St. Helens. J. Volcanol. Geotherm. Res. 24, 193–204.

Nakada, S., Motomura, Y., 1999. Petrology of the 1991–1995 eruption at Unzen; effusion pulsation and groundmass crystallization. J. Volcanol. Geotherm. Res. 89, 173–196.

Nakada, S., Shimizu, H., Ohta, K., 1999. Overview of the 1990–1995 eruption at Unzen Volcano. J. Volcanol. Geotherm. Res. 89, 1–22.

Rust, A.C., Manga, M., Cashman, K.V., 2002. Determining flow type, shear rate and shear stress in magmas from bubble shapes and orientations. J. Volcanol. Geotherm. Res. (in press).

Saar, M.O., Manga, M., Cashman, K.V., Fremouw, S., 2001. Numerical models of the onset of yield strength in crystal-melt suspensions. Earth Planet. Sci. Lett. 187, 367–379.

Stevens, N.F., Murray, J.B., Wadge, G., 1997. The volume and shape of the 1991–1993 lava flow field at Mount Etna, Sicily. Bull. Volcanol. 58, 449–454.

Stevens, N.F. et al., 2001. Surface movements of emplaced lava flows measured by synthetic aperture radar interferometry. J. Geophys. Res. 106, 11293–11313.

Varga, R.J., Bailey, R.A., Suemnicht, G.A., 1990. Evidence for 600 year-old basalt and magma mixing at Inyo Craters volcanic chain, Long Valley Caldera, California. J. Geophys. Res. 95, 21441–21450.

Wunderman, R., Venzke, E., Mayberry, G., Jensen, L., Charvonia, D., Gluck, J., 2000. Popocatépetl (Mexico) December set records in tremor, dome extrusion rates, SO_2 flux, and tilt. Bull. Glob. Volcan. Netw. 25, 2–5.

Young, S.R., White, R., Wadge, G., Voight, B., Toothill, J., Stevens, N., Stewart, R., Stasiuk, M., Sparks, R.S.J., Skerrit, J., Shepherd, J., Scott, W., Robertson, R., Power, J., Norton, G., Murphy, M., Miller, A., Miller, C.D., Lynch, L., Luckett, R., Lejeune, A.M., Latchman, J., James, M., Jackson, P., Hoblitt, R., Herd, R.A., Harford, C., Francis, P.W., Dyer, N., Druitt, T.H., Devine, J., Davies, M., Darroux, B., Cole, P., Calder, E.S., Barclay, J., Aspinall, S., Arafin, S., Ambeh, W., 1997. The ongoing eruption in Montserrat. Science 276, 371–372.